Geoderma 287 (2017) 71–79

Contents lists available at ScienceDirect

Geoderma

journal homepage: www.elsevier.com/locate/geoderma

Connectivity and percolation of structural pore networks in a cultivated silt loam soil quantified by X-ray tomography

Nicholas Jarvis *, Mats Larsbo, John Koestel

Department of Soil and Environment, Swedish University of Agricultural Sciences, Box 7014, 750 07 Uppsala, Sweden

ARTICLE INFO

Article history:
Received 1 February 2016
Received in revised form 10 June 2016
Accepted 24 June 2016
Available online 2 July 2016

Keywords:
Percolation
Connectivity
Macropore
X-ray tomography
Tilled soil

ABSTRACT

The connectivity of macropore networks is thought to exert an important control on preferential flow in soil, although little progress has been made towards incorporating an understanding of these effects into management-oriented flow and transport models. In principle, concepts from percolation theory should be well suited to quantify the connectivity of preferred flow pathways, but so far its relevance for natural soils in the field has not been tested. To investigate this question, X-ray tomography was used to measure soil pore space architecture at an image resolution of 65 μm for 64 samples taken in two consecutive years in the harrowed and ploughed layers of a silt loam soil a few weeks after spring cultivation. The results showed that the pore networks displayed key features predicted by classical percolation theory: a strong relationship was found between the percolating fraction and the imaged porosity, with a percolation threshold of ca. 0.04 to 0.06 m^3 m^{-3} in the harrowed layer. A percolation threshold was less clearly identifiable in topsoil that had not been recently tilled, although this may probably be attributed to finite size sampling effects in this layer, which showed a more heterogeneous and structured distribution of the pore space. Although further work on more strongly structured soil horizons, especially subsoils, would be desirable, it is tentatively suggested that percolation concepts could prove useful to estimate the conducting macroporosity in management models of preferential flow and transport.

1. Introduction

Soil structural pores (macropores) allow rapid and far-reaching preferential (i.e. non-equilibrium) flows of water, dissolved solutes and particulate matter, with potentially serious consequences for water quality (Jarvis, 2007). Application of non-invasive imaging techniques has revealed that macropores in soils generally form partially-connected networks of rather complex topology (e.g. Perret et al., 1999; Pierret et al., 2002; Mooney and Korošak, 2009; Luo et al., 2010a). It is also empirically quite well established that the connectivity of these macropore networks may strongly influence susceptibility to preferential flow at all scales ranging from columns through pedons to hillslopes (e.g. Noguchi et al., 1999; Luo et al., 2010b; Nieber and Sidle, 2010; Larsbo et al., 2014). The effects of this complex soil pore architecture on flow and transport can be captured by pore-scale modelling at small scales, either directly on X-ray imaged pore systems (e.g. Hyväluoma et al., 2012; Scheibe et al., 2015) or on simplified pore network models that statistically represent the real network (e.g. Köhne et al., 2011). However, with only a few exceptions (e.g. Klaus and Zehe, 2011), only limited progress has been made towards incorporating a quantitative treatment of macropore connectivity into models that are better suited to the much larger spatial and temporal scales relevant for management applications. For example, widely-used dual-permeability models (e.g. Šimůnek et al., 2003; Larsbo et al., 2005; Šimůnek and van Genuchten, 2008) that apply continuum flow equations in two interacting flow domains, implicitly assume that the larger pores comprising the preferential flow domain are perfectly connected. Simple yet realistic methods that can capture emergent effects of the connectivity of complex macropore networks on flow and transport at larger scales would therefore help progress towards more reliable model predictions.

In principle, concepts from percolation theory should be well suited to characterize the connectivity of preferred flow pathways (e.g. Western et al., 2001; Schlüter and Vogel, 2011; Renard and Allard, 2013). In hillslope hydrology, percolation concepts have been employed to understand and model both surface runoff (Darboux et al., 2002) and sub-surface downslope discharge above an irregular soil-rock boundary (Lehmann et al., 2007; Janzen and McDonnell, 2015) as a threshold response to precipitation influenced by the connectivity of topographic depressions along the slope. Nieber et al. (2006) suggested that percolation concepts might describe the connectivity of self-organized macropore networks in soil, but to our knowledge, this idea has not yet been pursued. Liu and Regenauer-Lieb (2011) used percolation concepts to analyze the pore structures of rock, bread and wood samples imaged by X-ray tomography, but we are not aware of any such

* Corresponding author.
E-mail address: nicholas.jarvis@slu.se (N. Jarvis).

http://dx.doi.org/10.1016/j.geoderma.2016.06.026

investigations on natural soils. In this study, we investigate whether percolation concepts can be used to describe the connectivity of structural pore networks in a tilled topsoil of a silt loam, as quantified by high-resolution industrial X-ray tomography (Helliwell et al., 2013).

2. Materials and methods

2.1. Field site and sampling

64 soil cores sampled in PVC cylinders each with an inner diameter of 6.7 cm and a length of 10 cm, were taken from a long-term field experiment located at Offer in northern Sweden (63.1°N, 17.8°E), which is described in more detail by Bolinder et al. (2010). The site has a mean annual average temperature of 3.4 °C and an annual precipitation of 567 mm (averages for period 1961–2000). Half of the samples were taken in June 2013 and the other half in June 2014. Each year, eight core samples were taken from each of four plots subjected to four different crop rotations established in 1956, which differed with respect to the number of years of grass ley in the rotation (1, 3, 4 or 5 years of grass ley in a six-year rotation, with arable crops in the remaining years). In both years, we sampled the four plots in the first year of arable cultivation after the break of the grass ley ca. 3 weeks after seedbed preparation (harrowing to a depth of ca. 6 cm) and sowing. The plots had been ploughed to a depth of ca. 20–25 cm the previous autumn. On each sampling occasion, 16 cores were sampled at the soil surface and 16 directly below them in the horizon which had been ploughed, but not harrowed.

The soil at Offer is a silt loam, with clay contents varying between 23 and 40% (with a mean of 30%) and silt contents between 50 and 68% (with a mean value of 57%). The long-term cropping treatments have affected the soil organic carbon contents (Bolinder et al., 2010), which varied between 1.3% and 4.1% among the sampled plots (with a mean value of 2.5%).

2.2. X-ray tomography and image analyses

2.2.1. X-ray scanning

We imaged the samples using the GE Phoenix X-ray scanner (v|tome|x 240), which is installed at the Department of Soil and

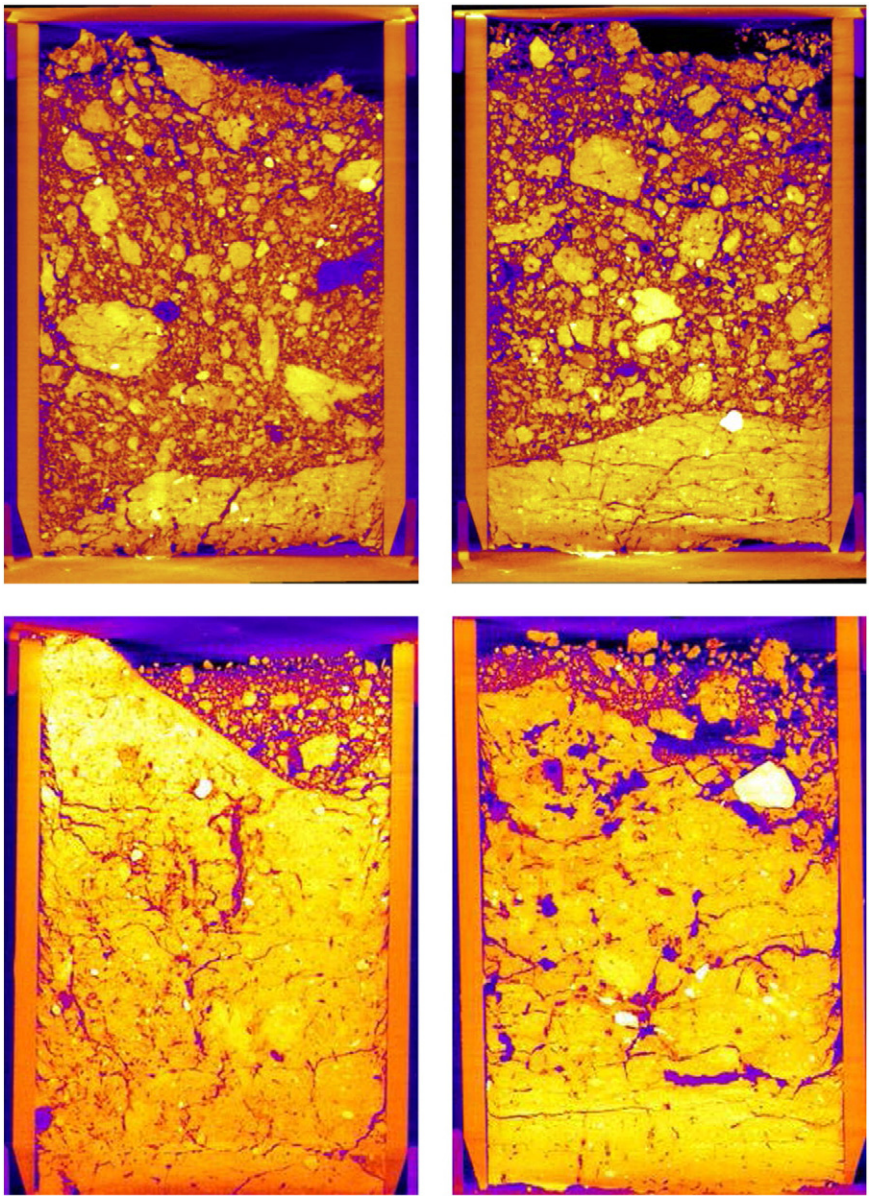

Fig. 1. Four example 2D images of vertical slices through samples (inner diameter 6.7 cm) taken at Offer, illustrating the contrasting structures in the harrowed and ploughed layers. The two uppermost images are samples taken from the soil surface, the two beneath are from 10 to 20 cm depth.

Environment at the Swedish University of Agricultural Sciences, Uppsala. The X-ray scanner is equipped with a tungsten target and a GE 16″ flat panel detector with 2024 × 2024 detector crystals. All scans were carried out at a tube-voltage of 200 kV and an electron flow of 400 μA. A 0.5 mm thick optical copper filter was used to harden the X-ray beam. 1800 radiographs were collected for each sample, each being the average of three repeated image acquisitions with an exposure time of 200 milliseconds. The radiograph data were then inverted to 3D X-ray images using the GE image reconstruction software datos|x. Each 3D image had a voxel resolution of 65 μm in all directions. The 16-bit monochrome images were saved in TIFF-format for further processing.

2.2.2. Image processing and segmentation

Image processing was accomplished using the open-source software ImageJ and the bundle of plugins distributed in FIJI (Schindelin et al., 2012). The images were first corrected for differences in illumination in the vertical direction assuming that the grey-values of the PVC walls were constant with depth. A 3D median filter with a radius of 2 voxels was then applied to reduce the noise in the images. Subsequently, an unsharp mask with standard deviation of one voxel and a weight of 0.7 was applied sequentially to each horizontal voxel layer to emphasize edges between individual structures in the images. Because the soil was relatively dry on both sampling occasions, all the visible pores in each sample were air-filled. We therefore first removed the regions with grey-scale values larger than or equal to the grey-scale value of the PVC wall. This left the less dense regions in the image which corresponded to air-filled pores, fresh organic matter and loose soil. We then selected a cylindrical region of interest that closely followed the inner diameter of the PVC cylinder. Next, we tried all the global thresholding methods available in ImageJ/Fiji on the lumped histogram of each 3D image to identify a global threshold. We validated the performance of each thresholding approach by visual inspection of three horizontal cross-sections, one located at one quarter, one in the middle and one at three-quarters of the height of each of the 64 imaged columns. Otsu's method (Otsu, 1979) gave acceptable segmentation results and was used to create binary images depicting pore and non-pore phases in each soil column.

2.2.3. Image analyses

2.2.3.1. Regions of interest (ROI). In a first step, we determined the topography of the top and bottom surfaces of each soil column. We then outlined three different regions of interest (ROI). The largest ROI corresponded to a cylindrical volume with its upper surface set 300 voxels (1.95 cm) below the median elevation of the soil surface. Its lower surface was set 615 voxels (4 cm) deeper. This was done to obtain an ROI which only contained soil from one horizon, since preliminary visual inspection of the images of the entire core samples showed that soil from two different horizons with very different pore structures was sometimes present in a sample. For example, soil from the horizon that had been ploughed but not harrowed was included at the base of many of the samples taken from the soil surface, while some of the samples nominally taken in the layer which had been ploughed but not harrowed included material from the harrowed layer at the surface or subsoil material at the base (see Fig. 1 for examples). The 78 voxels (5 mm) next to the column walls were cut away to avoid including possible wall artefacts introduced by sampling, leaving a cylinder 4 cm in height and 5.7 cm in diameter (volume of 102.1 cm^3). Hereafter, we refer to this volume as the 6 cm diameter cylindrical ROI. In order to perform a preliminary investigation of the effects of finite sample size on percolation, we also defined two additional ROI's. A cube of side-length 4 cm centered within the larger ROI described above was first defined. Each 4 cm cube was then sub-divided into eight cubes of side-length 2 cm (these are hereafter referred to as the 4 cm and 2 cm cubic ROI's respectively).

2.2.3.2. Percolation and pore network characteristics. Percolation theory was originally formulated in the 1950's as a mathematical theory of the connectivity of disordered (i.e. random) media (Stauffer and Aharony, 1992; Hunt et al., 2014). A basic concept underlying classical percolation theory is that a critical threshold value (the percolation threshold) of the occupancy probability (here, the macroporosity) is required to give long-range (effectively infinite) connectivity ("percolation"). In the context of percolation in a finite size system,

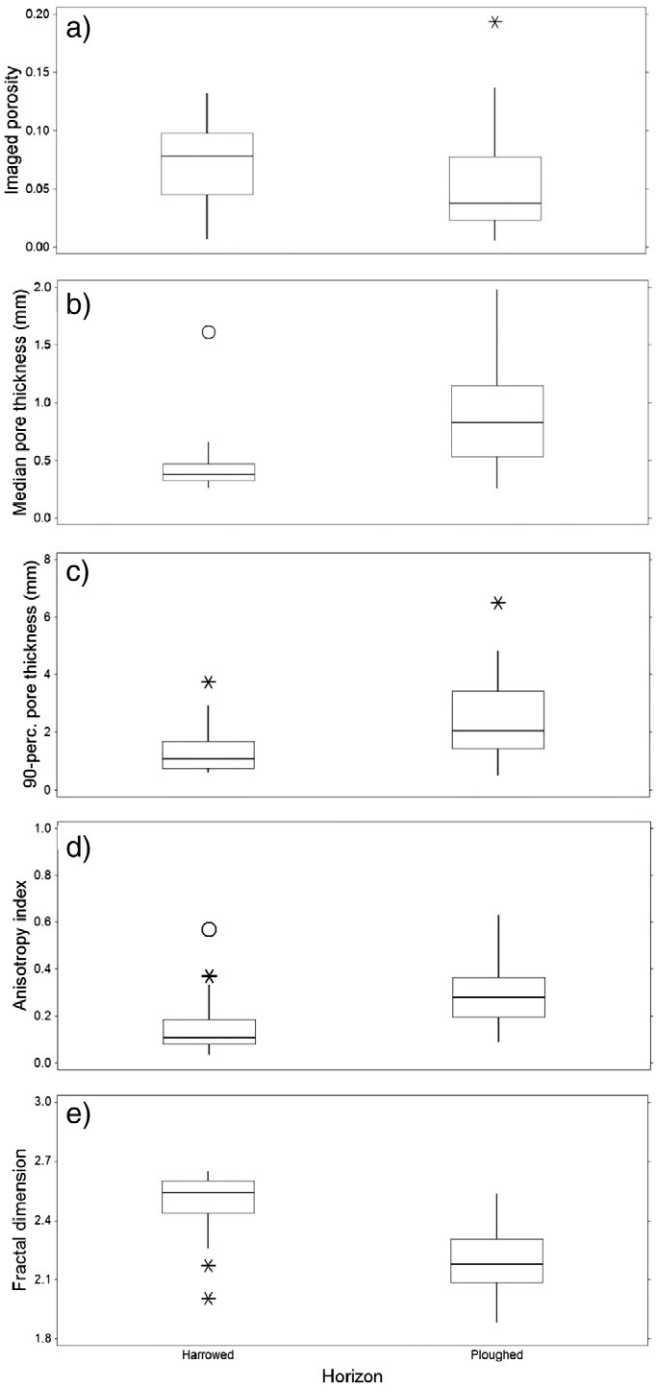

Fig. 2. Box and whisker plots for harrowed and ploughed horizons illustrating differences in a.) porosity, b.) median pore thickness, c.) 90th percentile pore thickness, d.) anisotropy index, and e.) fractal dimension. The horizontal lines indicate medians, the length of the box shows the inter-quartile range and whiskers indicate the range of typical values. Possible and probable outliers indicated by asterisks and open symbols are defined as values that lie outside the box boundaries by >1.5 and 3 times the size of the box respectively.

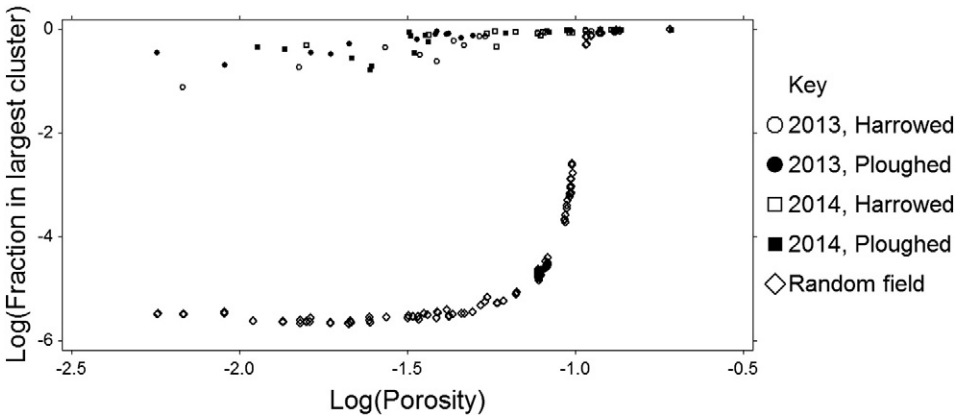

Fig. 3. The fraction of the pore space in the largest cluster as a function of porosity: a comparison of the imaged pore networks with random field realizations assuming 26NN.

connectivity can be estimated by the fraction of the pore space, F_p, that is connected across the ROI. We calculated the percolating pore space (i.e. connected to both the top and bottom of the sample) with the "Open and closed porosity" algorithm in the Porodict module of the GeoDict software (Math2Market GmbH, http://www.geodict.com). Connection between two voxels can be defined in different ways. For example, for a cubic grid, two voxels can be considered connected if they share a face (i.e. the six nearest neighbours, 6NN) or a face or an edge (18 nearest neighbours, 18NN), or at the extreme, they could be considered connected even if they only touch corners (twenty-six nearest neighbours, 26NN). We therefore investigated the effects of assuming 6NN and 26NN on the calculated percolating pore space in GeoDict.

The sizes of individual pores (i.e. connected "clusters" of pore voxels) were identified using the Particle Analyzer from the plugin BoneJ (Doube et al., 2010) to the software package ImageJ/FIJI (Schindelin et al., 2012). Two additional measures of connectivity of relevance for percolation (Hovadik and Larue, 2007; Renard and Allard, 2013) were derived from the sizes of these pore clusters, namely the proportion of the pore volume contained in the largest cluster, F_L, and the connection probability, Γ_p, which is defined as the probability that two randomly chosen pore voxels in the ROI are connected (i.e. they belong to the same cluster). Γ_p is given by:

$$\Gamma_p = \frac{\sum_i s_i(s_i-1)}{\sum_i s_i\left\{\left(\sum_i s_i\right)-1\right\}} \simeq \frac{\sum_i S_i^2}{\left(\sum_i s_i\right)^2} \quad (1)$$

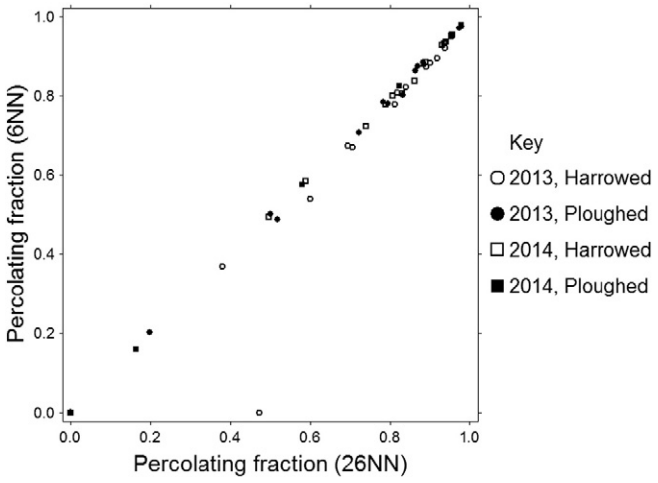

Fig. 4. The effects of the definition of connection on calculated percolating fractions (6NN = faces only; 26NN = faces, edges and corners).

where s_i is the size of pore cluster i expressed as the number of voxels. Similarly, the probability, P_L, of any two pore cells belonging to the largest pore cluster is given by:

$$P_L = \frac{s_L(s_L-1)}{\sum_i s_i\left\{\left(\sum_i s_i\right)-1\right\}} \simeq \frac{s_L^2}{\left(\sum_i s_i\right)^2} \quad (2)$$

where s_L is the size of the largest cluster. From Eq. (2), it can be seen that for large domains, P_L can be accurately estimated as F_L^2. Furthermore, if the total pore volume is dominated by a single large cluster (i.e. the largest cluster is much larger than all other individual clusters), then a comparison of Eqs. (1) and (2) shows that $\Gamma_p \approx F_L^2$. For a random structure above the percolation threshold in an ROI large enough to avoid finite size scaling effects, F_L should equal F_P since only the largest cluster percolates (Stauffer and Aharony, 1992). Analogous to Eq. (2), the probability for any two pore voxels to belong to the infinite percolation cluster can be estimated as F_p^2.

Percolation thresholds are significantly affected by structure (i.e. non-randomness) and heterogeneity in the pore network such as anisotropy (Ewing and Gupta, 1993; Liu and Regenauer-Lieb, 2011). The degree of anisotropy of the pore space was therefore computed in BoneJ using the mean intercept length method (Harrigan and Mann, 1984; Doube et al., 2010). This method gives an index of anisotropy which varies between zero and one, where zero represents a perfectly isotropic structure. In addition, as a measure of the heterogeneity and space-filling characteristics of the structural pore space, the mass fractal dimension was calculated with the box-counting algorithm implemented in BoneJ.

Connectivity of soil pore networks will also depend on the range of imaged pore sizes (Bird and Perrier, 2010). We therefore measured pore thickness distributions with the Porodict module of GeoDict. With this algorithm, pore thickness is determined by fitting spheres into the pore space. The pore thickness is defined for each pore voxel as the diameter of the largest sphere that fits into the macropore and contains the voxel (Hildebrand and Rüegsegger, 1997). In this paper, pore thickness distributions are summarized by the median and 90th percentile pore thicknesses. In addition to the percolating porosity, the range of pore sizes that percolate is also of great interest, since it should exert a significant control on preferential flow in a multi-scale porous medium like soil. For this reason, we also calculated the critical pore thickness, which is defined as the diameter of the largest sphere that can pass through the imaged pore system from top to bottom. This was calculated using an algorithm in GeoDict, whereby the imaged pore space is eroded one voxel at a time until connection (percolation) across the ROI is lost.

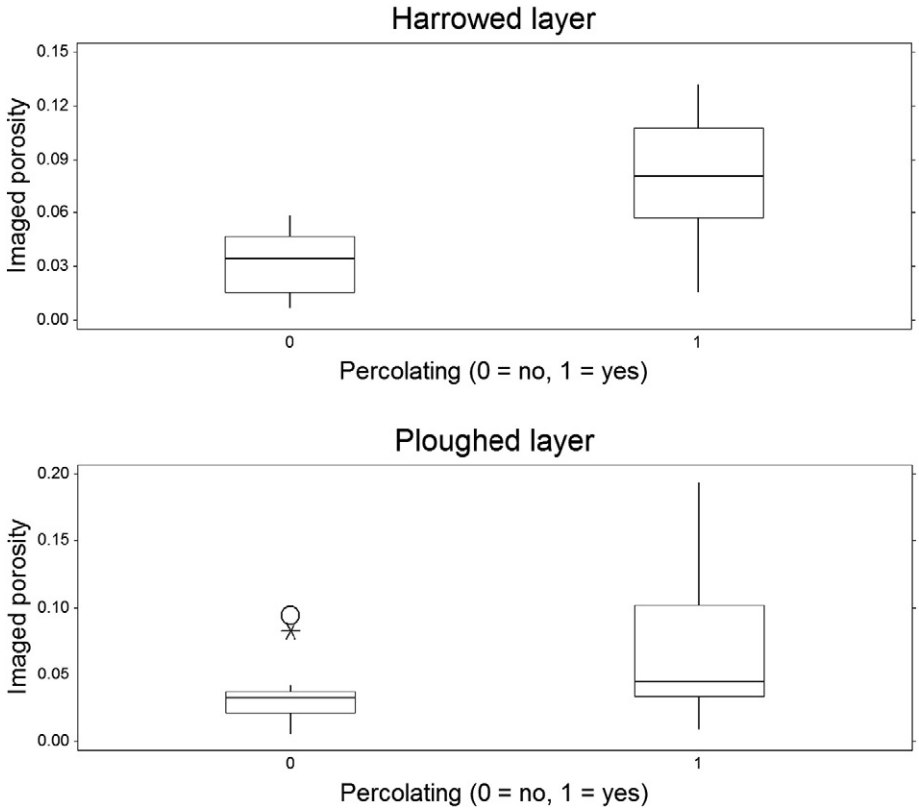

Fig. 5. Box and whisker plot showing imaged porosities for samples with and without percolating pore space. For explanations of symbols, see caption to Fig. 2.

2.3. Simulated random pore networks

We compared the connectivity of the X-ray imaged pore networks with that obtained for a simulated random system. To do this, we first created blank domains with the same dimensions and voxel size as the ROI's investigated in the soil columns. Random pore networks were created by iteratively assigning randomly selected voxels in the domain to the pore space until the desired porosity was reached. We simulated random fields with the same imaged porosities as the samples taken from the field, with between 2 and 5 replicates in each case. Random field realizations with >2 replicates correspond to porosities close to the expected percolation threshold of 0.1 for 26NN (Stauffer and Aharony, 1992). Pore network characteristics for the random fields were calculated in the same way as for the pore networks in the soil samples.

2.4. Statistics

Differences in the means of the various imaged pore space metrics between the two soil horizons and the two different sampling years were tested for statistical significance using two sample *t*-tests, testing for the homogeneity of variances. Relationships between pore space metrics were investigated with Pearson correlation coefficients. As noted above, the samples were taken from four different cropping

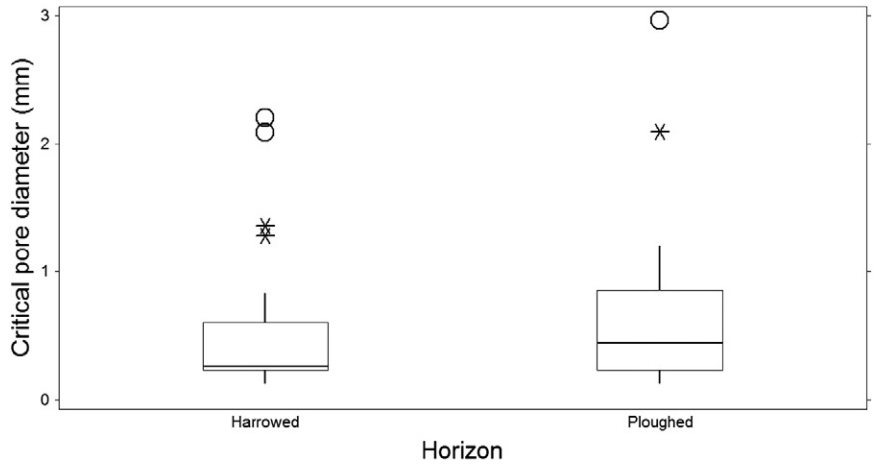

Fig. 6. Box and whisker plots of the critical pore thickness harrowed and ploughed horizons. For explanations of symbols, see Fig. 2.

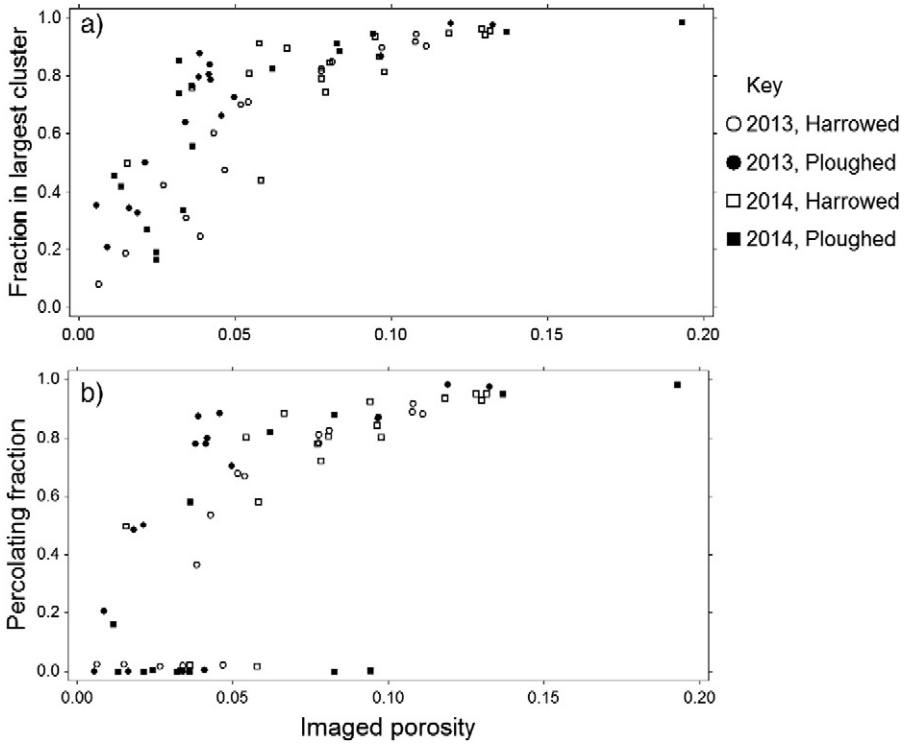

Fig. 7. Connectivity as a function of imaged porosity for, a.) F_L, the fraction of the porosity in the largest cluster, and b.) F_p, the percolating fraction (the fraction of the pore space connected between the top and bottom faces of the sample). To improve clarity, samples in the harrowed layer with no percolating porosity are plotted with a small positive value.

treatments. However, analyses with general linear mixed models showed that there were no significant effects of the crop treatments on the X-ray imaged pore metrics.

3. Results

3.1. Imaged porosity, pore size distribution and heterogeneity

Fig. 2a–e shows the imaged porosity and the measures of pore size distribution and heterogeneity in the 6 cm diameter cylindrical ROI for both harrowed and ploughed horizons. Fig. 2a–c shows that there is a tendency for the harrowed horizon to have larger imaged porosities ($p = 0.051$), smaller median pore sizes and fewer large macropores. The median pore thicknesses in most samples lie within the pore size range defined as macropores (>0.3–0.5 mm) by Jarvis (2007), even though the image resolution of 65 μm means that some smaller pores are included in the analysis. It can also be deduced from Fig. 2c that the local thickness of most of the imaged pore space ranges over a little more than one order of magnitude, with 90th percentile pore thicknesses for most samples varying between 1 and 3 mm. Finally, Fig. 2d,e demonstrate that the distribution of the pore space in the harrowed layer is significantly more isotropic and homogeneous than in the ploughed layer ($p \leq 0.0001$ for both the anisotropy index and fractal dimension).

3.2. Connectivity and percolation

Fig. 3 compares the measurements of F_L (the fraction of the porosity contained in the largest cluster) with the simulations for a random 6 cm diameter cylindrical domain, assuming 26NN in both cases. At very small imaged porosities (ca. 1 to 5%), the fraction of the pore space connected to the largest cluster in the field soil is more than four orders of magnitude larger than for the equivalent random networks, which is a simple demonstration of the strongly structured nature of these pore networks. Fig. 4 shows that choosing 26NN or 6NN has little effect on the fraction of the pore space that percolates for our samples. A large difference is found only for one sample with an imaged porosity of 0.047 $m^3\ m^{-3}$, which fails to percolate with 6NN, but has a percolating fraction of 0.47 with 26NN. For a random medium, the definition of connection strongly affects percolation. For example, for a sufficiently large cubic grid, the percolation thresholds are ca. 0.31 and 0.1 for 6NN and 26NN respectively (Stauffer and Aharony, 1992). In our data, the lack of sensitivity of percolation to the definition of connection is probably because the pore networks are strongly structured, although application of the median filter in the image processing may also have reduced the importance of corner connections.

For the 6 cm diameter cylindrical ROI, 43 of the 64 samples (25 in the harrowed layer and 18 in the ploughed) contained percolating pore networks for 6NN at the image resolution of 65 μm. Fig. 5 shows that for the harrowed layer, a percolation threshold can be clearly identified, since the sample means for percolating and non-percolating porosities are significantly different ($p = 0.002$). Although there is a greater overlap in the distributions of porosities for percolating and non-percolating pore networks in the ploughed layer, their means are still significantly different ($p = 0.037$). The percolation threshold (ca. 0.04–0.06 $m^3\ m^{-3}$ in the harrowed layer) is much smaller than the theoretical value for random fields of 31% for 6NN on a cubic grid which is sufficiently large to avoid the effects of the finite sample size (Stauffer and Aharony, 1992; Hunt et al., 2014). This is due to the structured nature of the pore space, which is known to strongly decrease percolation thresholds (e.g. Ewing and Gupta, 1993; Hovadik and Larue, 2007; Liu and Regenauer-Lieb, 2011).

The measurements of critical pore thickness (Fig. 6a,b) show that only a few samples contain large continuous macropores without any significant 'bottlenecks'. The critical pore thickness is smaller than the median thickness of the imaged pore space (Fig. 2b) for all but nine samples, while only six samples in the harrowed layer and eight in the ploughed would have percolating macroporosity at a lower cut-off pore thickness of 0.5 mm (Jarvis, 2007).

Fig. 7a shows how the fraction of the pore space in the largest cluster increases with porosity as the smaller macropore clusters merge into the dominant cluster. The highly significant linear correlation ($R^2 =$

0.998, $p < 0.0001$) between the connection probability, Γ_p, and F_L^2 (Fig. 8a) demonstrates that this largest cluster dominates the porosity in almost all samples (i.e. it is much larger than all other individual clusters). Fig. 8b shows that in all but five of the samples with percolating pore networks, the fraction of the porosity in the largest cluster is almost exactly equal to the percolating porosity, which implies that only the largest cluster percolates. However, in four samples there are two percolating clusters, while in another sample a small biopore spans the ROI but the largest pore cluster does not (see the inset images in Fig. 8b). These results demonstrate that the imaged porosity closely follows the behavior expected in classical mono-scale percolation, such that the percolating fraction of the pore space, F_p, is determined by the percolating porosity (Fig. 7b). Both connectivity metrics, F_p and F_L, show that the imaged pore space in the horizon which has been ploughed but not harrowed tends to have a greater connectivity at any given porosity (Fig. 7), which indicates that the pore space in this layer is more structured. In contrast, there are no apparent effects of sampling year on these connectivity functions, even though porosities tended to be smaller in 2013 than in 2014 in the harrowed layer ($p = 0.085$).

Fig. 9 compares the percolating pore fractions as a function of imaged porosity for the 2 cm and 4 cm cubes. In the harrowed horizon, the relationships between the percolating fractions and porosity for the two ROI's are similar, although the percolation threshold is slightly less well defined for the 2 cm cubes and there is more scatter in the percolating fraction for any given porosity. Fig. 9 shows more pronounced differences in the data obtained for the 2 cm and 4 cm cubes in the ploughed horizon. Some of the 2 cm sized cubes have very large percolating fractions at small porosities, while the opposite is true for others. In the ploughed horizon, the percolation threshold is even more poorly defined for the 2 cm cubes than for the 4 cm cubes, as evidenced by the much larger spread in the porosity values for samples that do not percolate (Fig. 9). It seems clear that the size of ROI required to avoid finite size effects is larger in the ploughed horizon, where the pore space is more structured and heterogeneously distributed. This is illustrated in Fig. 9 by the images for two ROI's, one with a small vertically-oriented biopore which is continuous from top to bottom through the sample, and another which contains a larger biopore which only connects laterally across the ROI. In this case, an apparent anisotropy in the pore space becomes evident because the ROI is smaller than the typical spacing of macropores.

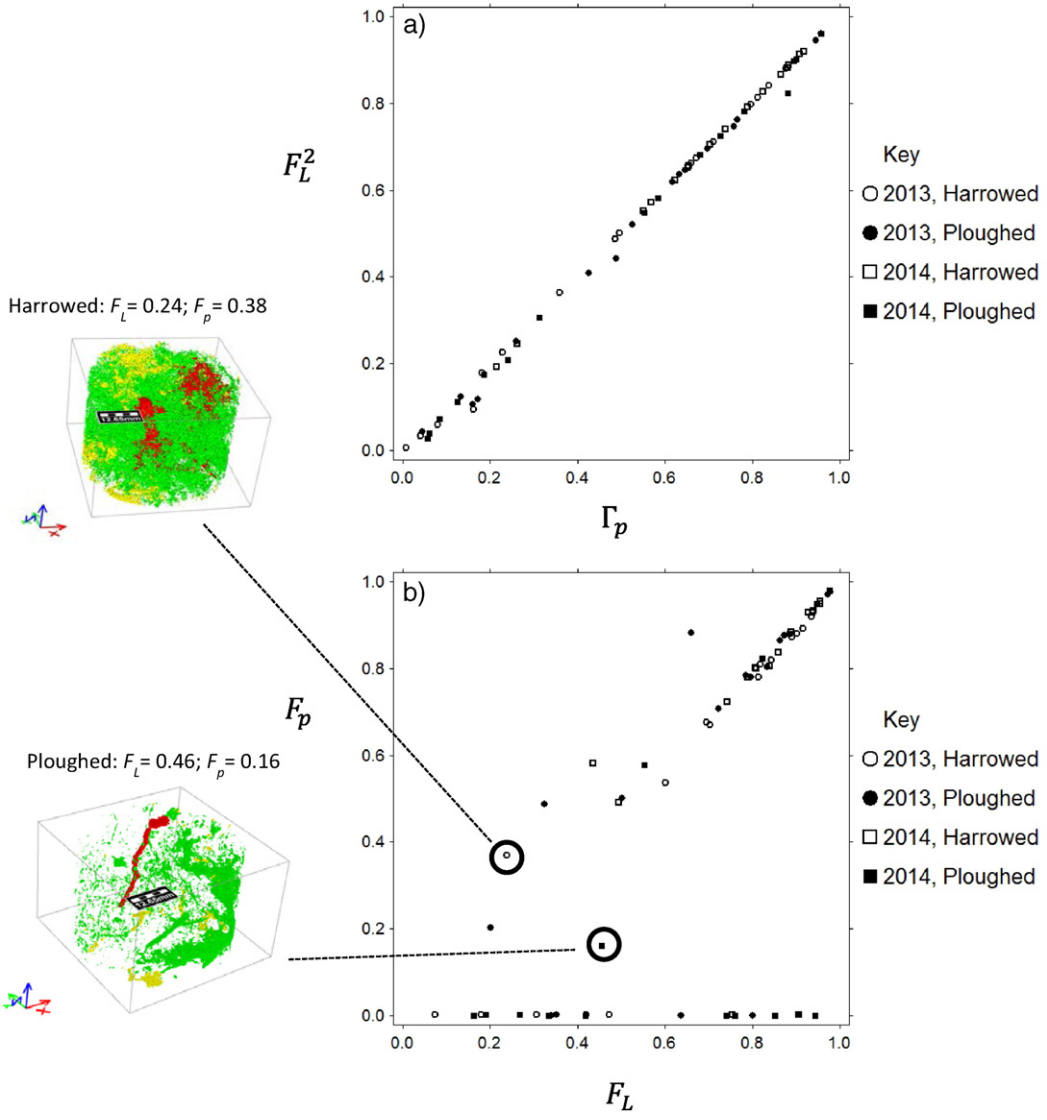

Fig. 8. The relationships among three connectivity metrics: the fraction of the pore space in the largest cluster, F_L, the connection probability, Γ_p and the percolating fraction of the pore space, F_p. Two example 3D images of the pore space are shown (red voxels are connected to both top and bottom faces, yellow voxels are connected to either the top or the bottom face, green voxels are disconnected from both top and bottom faces).

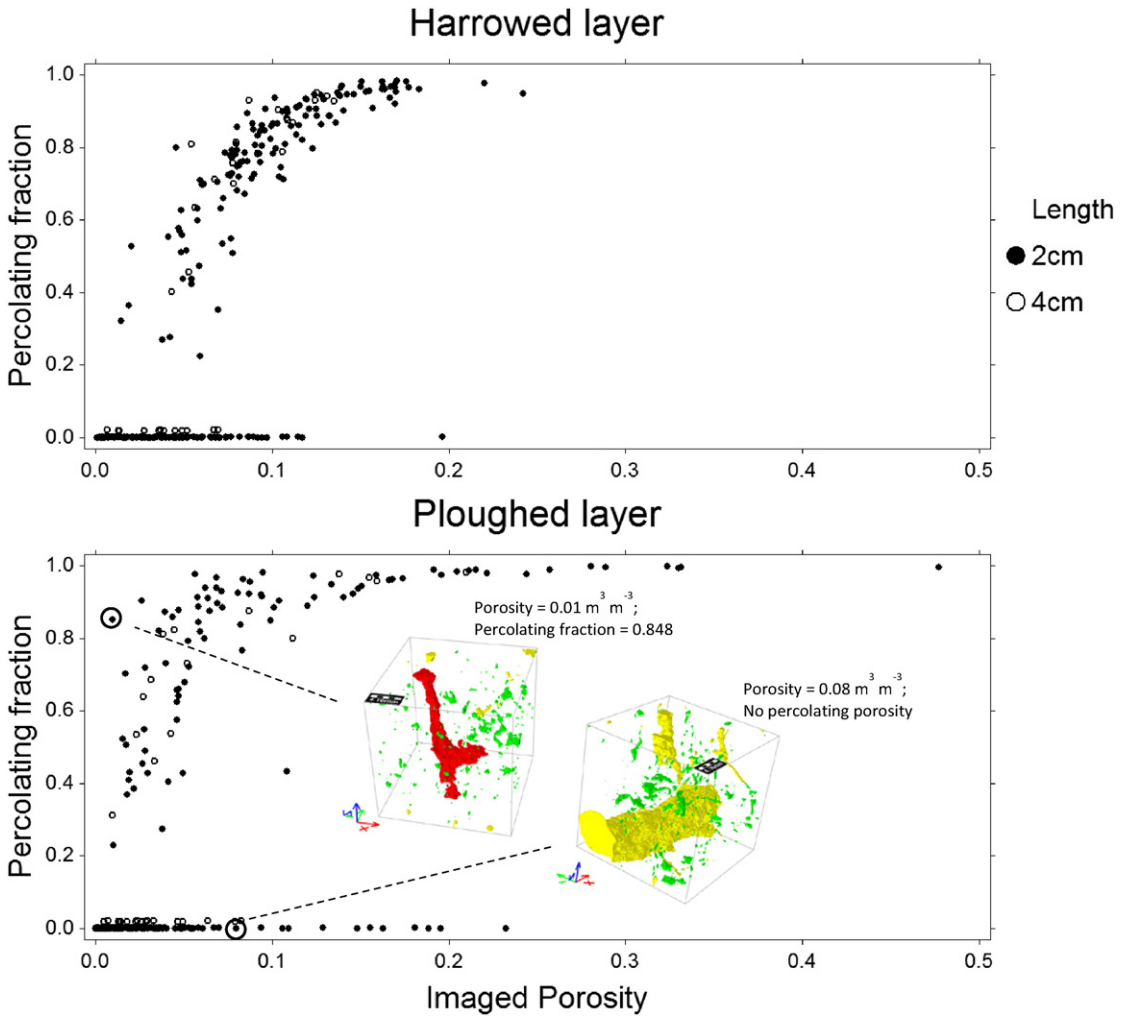

Fig. 9. Percolating pore fractions as a function of imaged porosity for 2 cm and 4 cm cubic ROI's in the harrowed and ploughed layers. Two example images of 2 cm cubic ROI's are shown (for an explanation of the colour coding of the pore space, see the caption to Fig. 8). To improve clarity, 4 cm cubes with no percolating porosity are plotted with a small positive value.

4. Discussion and conclusions

The structural porosity quantified by X-ray tomography in the topsoil of this cultivated silt loam soil displayed many of the key features predicted by classical percolation theory. In particular, a strong relationship was found between the percolating fraction and the imaged porosity, with a reasonably well-defined percolation threshold (ca. 0.04–0.06 m^3 m^{-3}), particularly in the harrowed layer. The percolation threshold was less well identified in the soil layer that had not been recently tilled, which we attributed to finite sample size effects resulting from the more heterogeneous distribution of structural pore space in this layer. Neither the different cropping treatments nor the sampling year had any significant effect on imaged pore network characteristics. The reasons for this are not clear, but it may be due to the timing of sampling, just a few weeks after spring cultivation in both years. More contrasting macropore structures may have become apparent later in the season due to the effects of various physical and biological structure-forming factors such as wetting and drying, root development and earthworm activity (e.g. Strudley et al., 2008).

The range of pore sizes that will allow significant non-equilibrium conditions to develop during flow is still a matter of some debate, especially for unsaturated conditions in the field (Nimmo, 2012; Beven and Germann, 2013). However, it does seem reasonable to conclude that most of our columns would be unlikely to exhibit very pronounced preferential flow due to a lack of percolating larger macropores, especially in the recently harrowed layer. This is in agreement with the results of many field tracer and dye staining experiments reported in the literature (Jarvis, 2007). The applicability of percolation concepts to describe the connectivity of macropore networks in more strongly structured soil susceptible to preferential flow (e.g. undisturbed subsoils) should therefore be investigated, although application of X-ray imaging for samples representative of the spatial scale of the structure might be problematic in many cases. Macropore networks in subsoil horizons are likely to be more anisotropic than the tilled layers studied here, since they are often dominated by root and macro-faunal biopores (Jarvis, 2007; Luo et al., 2010a). Percolation thresholds for such strongly anisotropic pore networks may be close to zero, with multiple disconnected percolating clusters and percolating fractions that approach unity even at small porosities (Ewing and Gupta, 1993; Liu and Regenauer-Lieb, 2011).

Dual-permeability models (e.g. Šimůnek et al., 2003; Larsbo et al., 2005; Šimůnek and van Genuchten, 2008) describe preferential flow as a threshold-driven hydrological process, whereby water pressures must locally exceed a critical value close to saturation to generate flow in macropores (Jarvis, 2007; Zehe and Sivapalan, 2009; Cey and Rudolph, 2009). Our results suggest that a second threshold process related to percolation may also operate in that a critical value of the macroporosity may be needed to ensure the long-range connectivity of the network and sustain far-reaching preferential flow through the unsaturated zone. This suggests that dual-permeability models could

be further developed by defining the conducting part of the macropore network as a dynamic function of soil wetness in an analogous way to "fill and spill" models of hillslope runoff (e.g. Lehmann et al., 2007; Janzen and McDonnell, 2015). In this respect, we only measured the percolating fraction of the macroporosity, while the potentially conducting "backbone" part of the macropore network will be even smaller due to "dead-end" macropores. The conducting backbone fraction of the macroporosity could be identified either by flow simulations on the imaged networks or directly measured by X-ray tomography during flow and transport experiments (e.g. Luo et al., 2008; Koestel and Larsbo, 2014; Sammartino et al., 2015).

Acknowledgements

This work was carried out in the project "Pore network characteristics and preferential transport in cultivated soil" funded by the Swedish Research Council Formas, grant number 220-2012-572. We thank Lars Gradin at Lantmännen, Lännes, for guidance during sampling at the field site at Offer. We would also like to thank Jürgen Becker and Jens-Oliver Schwarz at Math2Market for their help and support in the use of Geodict software.

References

Beven, K., Germann, P., 2013. Macropores and water flow in soils revisited. Water Resour. Res. 49, 3071–3092.
Bird, N.R.A., Perrier, E., 2010. Multiscale percolation properties of a fractal pore network. Geoderma 160, 105–110.
Bolinder, M.A., Kätterer, T., Andrén, O., Ericson, L., Parent, L.-E., Kirchmann, H., 2010. Long-term soil organic carbon and nitrogen dynamics in forage-based crop rotations in northern Sweden (63–64°N). Agric. Ecosyst. Environ. 138, 335–342.
Cey, E.E., Rudolph, D.L., 2009. Field study of macropore flow processes using tension infiltration of a dye tracer in partially saturated soils. Hydrol. Proc. 23, 1768–1779.
Darboux, F., Davy, P., Gascuel-Odoux, C., 2002. Effect of depression storage capacity on overland-flow generation for rough horizontal surfaces: water transfer distance and scaling. Earth Surf. Process. Landf. 27, 177–191.
Doube, M., Klosowski, M.M., Arganda-Carreras, I., Cordelieres, F.P., Dougherty, R.P., Jackson, J.S., et al., 2010. BoneJ: free and extensible bone image analysis in ImageJ. Bone 47, 1076–1079.
Ewing, R.P., Gupta, S.C., 1993. Percolation and permeability in partially structured networks. Water Resour. Res. 29, 3179–3188.
Harrigan, T.P., Mann, R.W., 1984. Characterization of microstructural anisotropy in orthotropic materials using a second rank tensor. J. Mater. Sci. 19, 761–767.
Helliwell, J.R., Sturrock, C.J., Grayling, K.M., Tracy, S.R., Flavel, R.J., Young, I.M., Whalley, W.R., Mooney, S.J., 2013. Applications of X-ray computed tomography for examining biophysical interactions and structural development in soil systems: a review. Eur. J. Soil Sci. 64, 279–297.
Hildebrand, T., Rüegsegger, P., 1997. A new method for the model-independent assessment of thickness in three-dimensional images. J. Microscopy 185, 67–75.
Hovadik, J.M., Larue, D.K., 2007. Static characterizations of reservoirs: refining the concepts of connectivity and continuity. Pet. Geosci. 13, 195–211.
Hunt, A., Ewing, R., Ghanbarian, B., 2014. Percolation Theory for Flow in Porous Media. Lecture Notes in Physics 880. third ed. Springer, Heidelberg.
Hyväluoma, J., Thapaliya, M., Alaraudanjoki, J., Sirén, T., Mattila, K., Timonen, J., Turtola, E., 2012. Using microtomography, image analysis and flow simulations to characterize soil surface seals. Comput. Geosci. 48, 93–101.
Janzen, D., McDonnell, J.J., 2015. A stochastic approach to modelling and understanding hillslope runoff connectivity dynamics. Ecol. Model. 298, 64–74.
Jarvis, N.J., 2007. Review of non-equilibrium water flow and solute transport in soil macropores: principles, controlling factors and consequences for water quality. Eur. J. Soil Sci. 58, 523–546.
Klaus, J., Zehe, E., 2011. A novel explicit approach to model bromide and pesticide transport in connected soil structures. Hydrol. Earth Syst. Sci. 15, 2127–2144.
Koestel, J., Larsbo, M., 2014. Imaging and quantification of preferential solute transport in soil macropores. Water Resour. Res. 50, 4357–4378.
Köhne, J.M., Schlüter, S., Vogel, H.-J., 2011. Predicting solute transport in structured soil using pore network models. Vadose Zone J. 10, 1082–1096.
Larsbo, M., Roulier, S., Stenemo, F., Kasteel, R., Jarvis, N.J., 2005. An improved dual-permeability model of water flow and solute transport in the vadose zone. Vadose Zone J. 4, 398–406.
Larsbo, M., Koestel, J., Jarvis, N.J., 2014. Relations between macropore network characteristics and the degree of preferential solute transport. Hydrol. Earth Syst. Sci. 18, 5255–5269.
Lehmann, P., Hinz, C., McGrath, G., Tromp-van Meerveld, H.J., McDonnell, J.J., 2007. Rainfall threshold for hillslope outflow: an emergent property of flow pathway connectivity. Hydrol. Earth Syst. Sci. 11, 1047–1063.
Liu, J., Regenauer-Lieb, K., 2011. Application of percolation theory to microtomography of structured media: percolation threshold, critical exponents, and upscaling. Phys. Rev. E 83, 016106.
Luo, L., Lin, H., Halleck, P., 2008. Quantifying soil structure and preferential flow in intact soil using X-ray computed tomography. Soil Sci. Soc. Am. J. 72, 1058–1069.
Luo, L., Lin, H., Li, S., 2010a. Quantification of 3-D soil macropore networks in different soil types and land uses using computed tomography. J. Hydrol. 393, 53–64.
Luo, L., Lin, H., Schmidt, J., 2010b. Quantitative relationships between soil macropore characteristics and preferential flow and transport. Soil Sci. Soc. Am. J. 74, 1929–1937.
Mooney, S.J., Korošak, D., 2009. Using complex networks to model two- and three-dimensional soil porous architecture. Soil Sci. Soc. Am. J. 73, 1094–1100.
Nieber, J.L., Sidle, R.C., 2010. How do disconnected macropores in sloping soils facilitate preferential flow? Hydrol. Proc. 24, 1582–1594.
Nieber, J.L., Steenhuis, T.S., Walter, T., Bakker, M., 2006. Enhancement of seepage and lateral preferential flow by biopores on hillslopes. Biologia 61, S225–S228.
Nimmo, J., 2012. Preferential flow occurs in unsaturated conditions. Hydrol. Proc. 26, 786–789.
Noguchi, S., Tsuboyama, Y., Sidle, R.C., Hosoda, I., 1999. Morphological characteristics of macropores and the distribution of preferential flow pathways in a forested slope segment. Soil Sci. Soc. Am. J. 63, 1413–1423.
Otsu, N., 1979. Threshold selection method from gray-level histograms. Ieee Trans. Syst. Man and Cybern. 9, 62–66.
Perret, J., Prasher, S.O., Kantzas, A., Langford, C., 1999. Three-dimensional quantification of macropore networks in undisturbed soil cores. Soil Sci. Soc. Am. J. 63, 1530–1543.
Pierret, A., Capowiez, Y., Belzunces, L., Moran, C.J., 2002. 3D reconstruction and quantification of macropores using X-ray computed tomography and image analysis. Geoderma 106, 247–271.
Renard, P., Allard, D., 2013. Connectivity metrics for subsurface flow and transport. Adv. Water Resour. 51, 168–196.
Sammartino, S., Lissy, A.-S., Bogner, C., van den Bogaert, R., Capowiez, Y., Ruy, S., Cornu, S., 2015. Identifying the functional macropore network related to preferential flow in structured soils. Vadose Zone J. http://dx.doi.org/10.2136/vzj2015.05.0070.
Scheibe, T.D., Perkins, W.A., Richmond, M.C., McKinley, M.I., Romero-Gomez, P.D.J., Oostrom, M., Wietsma, T.W., Serkowski, J.A., Zachara, J.M., 2015. Pore-scale and multiscale numerical simulation of flow and transport in a laboratory-scale column. Water Resour. Res. 51, 1023–1035.
Schindelin, J., Arganda-Carreras, I., Frise, E., Kaynig, V., Longair, M., Pietzsch, T., et al., 2012. Fiji: an open-source platform for biological-image analysis. Nat. Methods 9, 676–682.
Schlüter, S., Vogel, H.-J., 2011. On the reconstruction of structural and functional properties in random heterogeneous media. Adv. Water Resour. 34, 314–325.
Šimůnek, J., van Genuchten, M.T., 2008. Modeling nonequilibrium flow and transport processes using HYDRUS. Vadose Zone J. 7, 782–797.
Šimůnek, J., Jarvis, N.J., van Genuchten, M.T., Gärdenäs, A., 2003. Review and comparison of models for describing nonequilibrium and preferential flow and transport in the vadose zone. J. Hydrol. 272, 14–35.
Stauffer, D., Aharony, A., 1992. Introduction to Percolation Theory (2nd Edition). Taylor and Francis, London.
Strudley, M.R., Green, T.R., Ascough II, J.C., 2008. Tillage effects on soil hydraulic properties in space and time: state of the science. Soil Tillage Res. 99, 4–48.
Western, A., Blöschl, G., Grayson, R.B., 2001. Toward capturing hydrologically significant connectivity in spatial patterns. Water Resour. Res. 37, 83–97.
Zehe, E., Sivapalan, M., 2009. Threshold behavior in hydrological systems as (human) geo-ecosystems: manifestations, controls, implications. Hydrol. Earth Syst. Sci. 13, 1273–1297.